Soft Matter

Cite this: *Soft Matter*, 2012, **8**, 10486

www.rsc.org/softmatter

PAPER

Topological rearrangements and stress fluctuations in quasi-two-dimensional hopper flow of emulsions

Dandan Chen,* Kenneth W. Desmond and Eric R. Weeks

Received 2nd May 2012, Accepted 17th August 2012
DOI: 10.1039/c2sm26023a

We experimentally study the shear flow of oil-in-water emulsion droplets in a thin sample chamber with a hopper shape. In this thin chamber, the droplets are quasi-2D in shape. The sample is at an area fraction above jamming and forced to flow with a constant flux rate. Stresses applied to a droplet from its neighbors deform the droplet outline, and this deformation is quantified to provide an *ad hoc* measure of the stress. As the sample flows through the hopper we see large fluctuations of the stress, similar in character to what has been seen in other flows of complex fluids. Periods of time with large decreases in stress are correlated with bursts of elementary rearrangement events ("T1 events" where four droplets rearrange). More specifically, we see a local relationship between these observations: a T1 event decreases the inter-droplet forces up to 3 droplet diameters away from the event. This directly connects microscopic structural changes to macroscopic fluctuations, and confirms theoretical pictures of local rearrangements influencing nearby regions. These local rearrangements are an important means of reducing and redistributing stresses within a flowing material.

1 Introduction

Newtonian fluids at low flow rates flow laminarly, with the flow field independent of time. In contrast, complex materials such as sand, foam, and emulsions behave like elastic solids at rest, and under sufficient applied stress, they flow. While such materials have well defined time-averaged stresses and velocity fields, their flows have strong stress fluctuations even at low flow rates.[1–5] This macroscopic observation is not surprising as microscopically the individual grains (or bubbles or droplets) in a material must rearrange to allow for flow,[6] and their discrete size gives rise to these fluctuations. These rearrangements often occur in spatially heterogeneous fashion.[2–5] Inter-particle forces are also spatially heterogeneous, with a small subset of particles bearing large forces, as has been seen in experiments studying granular materials,[7,8] emulsion droplets,[9,10] foams,[11] and simulations of frictionless particles.[12] It is likely that small rearrangements of these force-bearing particles influence stresses over a larger region.

A variety of experiments have elaborated on this overall picture of local rearrangements leading to macroscopic stress fluctuations. In particular, flowing foams have been quite useful. Some experiments studied dry foams in 2D:[13–18] these are foams with bubble area fraction $\phi > 0.95$, where the bubbles are deformed into polygonal shapes. Elastic stresses can be determined from the foam images, but this works only because of the polygonal shapes; this analysis is not applicable to wetter foams (lower area fractions) where the bubbles have rounder shapes.[14,18] These dry foam experiments revealed many interesting behaviors, for example correlations between rearrangement events and gradients in the mean flow velocity,[14] and asymmetries between contracting flows and expanding flows.[18] Other experiments studied wet 2D foams.[3,4,6,19–23] Due to imaging limitations, these experiments could not measure local stresses, only strain fields. Key observations from these experiments included observations of clusters of rearranging bubbles,[3,19] some understanding of how the mean velocity field relates to the macroscopic rheology,[4,20–23] and connections between instantaneous motions and time-averaged motions.[4] In general, these experiments focused on collections of rearrangement events and their relation to macroscopic stresses. Macroscopic stresses lead to average macroscopic strain profiles, which in turn cause collections of microscopic rearrangements that help the sample relax the macroscopic stress. The connection between individual local rearrangements and the relaxation of the stress has been difficult to see directly in experiments although conceptually it is clear such a link must exist.

Motivated by these experiments, theoretical work attempted to connect these microscopic (particle-scale) forces and rearrangements to the macroscopic stress fluctuations[1,3,24,25] and time-averaged velocity profiles.[20,26] Some theories[20,25–27] and simulations[28] make connections between individual microscopic rearrangements, the local stress field, and the macroscopic flow. The general picture from these theories is that stress builds up locally, eventually exceeding a local yield stress, leading to local rearrangements (perhaps in a cascade of several local events), which in turn relax the stress. These local events sum together to

Department of Physics, Emory University, Atlanta, GA 30322, USA. E-mail: dchen361@163.com

give macroscopic stress fluctuations. In particular, a specific prediction is that individual rearrangement events relax the stress *locally*.[26,28] This has not be directly tested in an experiment, due to the difficulty of measuring both bubble positions and stresses simultaneously. Understanding the details of such localized rearrangements may help us understand phenomena such as shear-banding[29] and flow of complex fluids in general.[20,26]

In this manuscript, we present experimental results of a "wet" oil-in-water emulsion where we can infer the stress on every oil droplet, and relate individual rearrangements to stress changes both locally and globally. Our experiment uses quasi-two-dimensional emulsion droplets. Small oil droplets are compressed between two parallel glass plates, deforming them into disks similar to experiments with photoelastic disks[7,8] or quasi-two-dimensional foams in Hele-Shaw cells.[11,18,23,25,28] Our samples are jammed, and the stress each droplet feels is quantified by examining each droplet's deviation from a circular shape. In this experiment, we directly and simultaneously observe macroscopic flow profiles, microscopic rearrangement events, and macroscopic and microscopic stresses. In particular, we study microscopic "T1 events," where four droplets exchange neighbors, as shown in Fig. 1(a–c).[3,4,6,14,25,28] During a T1 event, two neighboring droplets move apart and are no longer neighbors, while two other adjacent droplets move together and become neighbors: this is a change in topology. These rearrangements are induced by flowing the sample through a hopper [Fig. 1(d)].[5,24,30] We find that T1 events diminish the stresses felt by droplets over a distance up to ~3 diameters away from the event, demonstrating the existence of a flow cooperativity length scale, and showing how local rearrangements are responsible for macroscopic stress fluctuations as predicted theoretically.[26,28]

2 Experimental methods

Our droplets are silicon oil (poly-dimethylsiloxane, ρ = 1 g mL^{-1}, η = 350 mPa s) in water, stabilized by Fairy™ soap of mass fraction 0.025, and are produced with the "co-flow" microfluidic technique.[31] Our choice of emulsions (rather than foams) is for two main reasons: to avoid coarsening and to enable use of the microfluidic technique to control droplet sizes. Additionally, this is a new experimental system to complement prior experiments that studied granular media and foams. We place the droplets into quasi-two-dimensional hoppers shaped using a thin film of tape with thickness 0.10 ± 0.02 mm. The tape is sandwiched between two glass slides. The walls are sufficiently clean that droplets do not have their contacts pinned to the wall, as can be seen by observing the easy motion of droplets in a dilute sample when the sample chamber is tilted. Moving droplets do experience viscous forces from the walls (and each other), although these are generally weak enough that they do not deform the droplets directly.[32] In our experiment, these viscous forces are smaller than the inter-droplet forces.[32] This is because our flow rates are small (leading to smaller viscous forces) and our area fractions are large (leading to larger inter-droplet forces). Nonetheless, larger droplets will certainly experience larger viscous forces from the walls, and likewise droplets moving faster will experience larger viscous forces.

A constant flux rate is set by a syringe pump. This pump is attached to the far left edge of the flow chamber, which is

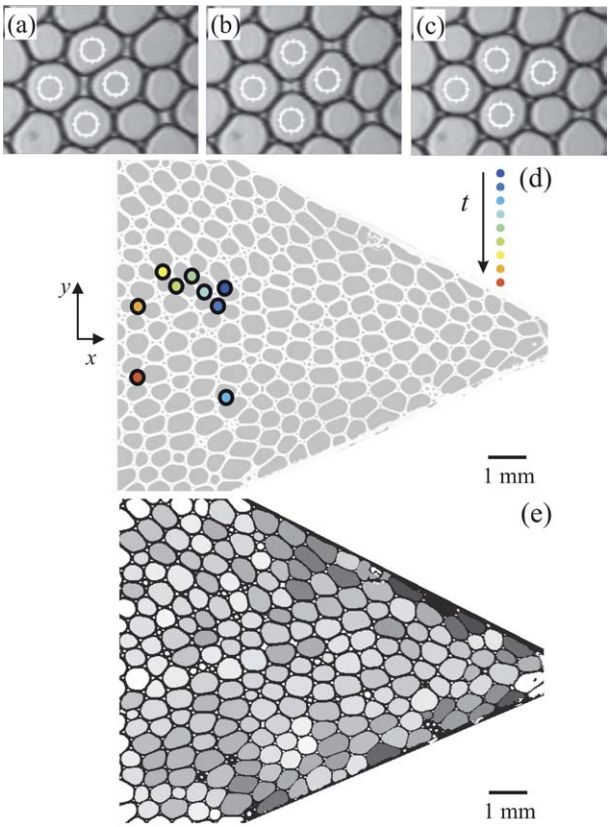

Fig. 1 (a)–(c) The three images show a typical T1 rearrangement of the four particles labeled by white circles. The field of view is 1.6 × 1.2 mm^2, and the time interval between consecutive images is 0.66 s; images from Run 1. (d) Snapshot of sample. The field of view is 11.2 × 8.5 mm^2. The flow direction is from left to right. The colored circles show the positions of T1 events taken from the time sequence of Fig. 2(b), where the earliest color (dark blue) corresponds to the T1 event at t = 38.7 s and the latest color (red) corresponds to the event at t = 47.3 s. Five of these T1 events occur in the time window t = (44.5 s, 46.2 s) during which the droplets in that region move downstream only 0.5 mm; these five events are the leftmost events of the top group shown in the image. The background image, taken at t = 45.2 s, has been inverted for better visualization. Each T1 event is positioned at the center of the four droplets comprising the T1 event based on their positions at t = 45.2 s. The data correspond to Run 1. (e) This image corresponds to (d), and is shaded based on the deformation D of each droplet. The darkest droplets correspond to D = 0.4 and white corresponds to D = 0.

~50 mm to the left of the images of Fig. 1(d and e). The chamber has parallel walls for ~40 mm, and then begins to contract in the hopper region. It is this contracting portion imaged in the figure; note that the left region visible in the figure has parallel edges due to the limited field of view, but nonetheless the entire field of view is well within the contraction region of the chamber. The mean velocity profile in this region is discussed below. We image the droplets with a 1.6× objective on an inverted microscope, using a 30 frame per s camera and a 0.33× camera-mount for a large field of view. The flow rates are sufficiently slow compared to the camera rate that the droplets can be individually tracked using standard routines.[33]

The details for our six experimental runs are given in Table 1. The samples have area fractions $\phi \geq 0.90$. At these high area

Table 1 Sample details of our six runs. The columns are flux rate A (mm^2 s^{-1}), normalized flux rate $\tilde{A} = A/\pi\langle r\rangle^2$ (s^{-1}), area fraction ϕ, mean droplet radius $\langle r\rangle$ (mm), standard deviation $\sigma = \sqrt{\left\langle (r-\langle r\rangle)^2 \right\rangle}$ normalized by $\langle r\rangle$, skewness $s = \left\langle \left(\frac{r-\langle r\rangle}{\sigma}\right)^3 \right\rangle$, hopper angle Θ (degrees), and length scale $\lambda/\langle r\rangle$

Run	A	$\tilde{A}$	ϕ	$\langle r\rangle$	$\sigma/\langle r\rangle$	s	Θ	$\lambda/\langle r\rangle$
1	2.93	12.8	0.90	0.27	0.21	0.010	25	2.9
2	1.33	18.8	0.90	0.15	0.17	−0.009	25	3.2
3	0.83	5.5	0.92	0.22	0.27	−0.010	27	3.8
4	0.75	14.1	0.93	0.13	0.24	−0.007	27	3.4
5	0.61	9.9	0.91	0.14	0.21	−0.010	26	3.0
6	0.33	6.2	0.94	0.13	0.28	−0.002	27	3.2

fractions, all of our samples are in the jammed state.[4,12] We find for our polydisperse samples that jamming occurs around $\phi_J \approx 0.84$: for $\phi < \phi_J$, surface tension ensures the droplets are perfectly circular, whereas for our experiments conducted at $\phi \approx 0.90$, all of the droplets are slightly deformed even at rest. The standard deviation of the droplet radii is sufficiently large in all cases to frustrate long-range order. Our results depend only on the mean radius $\langle r\rangle$ as will be described below, and do not otherwise change with different size distributions.

3 Results and discussion

3.1 Time-averaged velocity profiles

Like the flow of other jammed materials,[4,6,7,20,25] our time-averaged flow is smooth despite the complex motions of the individual droplets. The velocity profile described by

$$V_x(x,y) = \alpha(x) + \beta(x)y^2, \tag{1}$$

where $y = 0$ is the centerline of the channel, α is the flow rate along the centerline, and β relates to the local strain rate. Droplets at the side walls slip along the wall with the velocity of $V_x\left(x, \frac{w(x)}{2}\right) > 0$, where $w(x)$ is the channel width that droplet centers can reach. The parameters α and β are proportional to the flux rate A as

$$\alpha = \frac{k_\alpha A}{\left(w(x) + 2\langle r\rangle\right)}, \beta = \frac{-k_\beta A}{\left(w^3(x) + 6\langle r\rangle w^2(x)\right)}. \tag{2}$$

Eqn (1) and (2), and parameters $k_\alpha = 1.24$ and $k_\beta = 2.87$ are all empirical observations. We find $V_y \sim 0.1 V_x$ in all regions within the sample chamber. The equations above ensure† that the flux rate A is independent of position x. Our parabolic flow profiles are similar to those due to finite size effects seen in prior experiments, and likely reflect the finite size of our hopper.[20] We emphasize that eqn (1) describes the time-average flow, and that the instantaneous velocity field can be and usually is different.

† The total flux rate $A(x)$ is given by $A(x) = \int_{-(w(x)/2)}^{(w(x)/2)} V_x(x,y)\mathrm{d}y + 2V_x\left(y = \frac{w}{2}\right)\langle r\rangle$, where the second term accounts for slip of droplets along the wall. Using eqn (1) and (2), $A(x) = (k_\alpha - k_\beta/12)A = A$. That is, we only have one fit parameter, k_β, as $k_\alpha = 1 + k_\beta/12$ to ensure constant (x-independent) flux.

3.2 Global stress fluctuations *vs.* T1 frequency

To quantify stress fluctuations in the flowing sample, we first examine the shapes of individual droplets to determine their stresses. Droplets are deformed away from perfect circles by forces from neighboring droplets.[9,10] We quantify the deformation by determining the outline of each droplet, finding the radius r at each point on the outline (measured from the center of mass of the droplet), and then defining the droplet deformation

$$D = \sqrt{\langle r^2\rangle - \langle r\rangle^2/\langle r\rangle}, \tag{3}$$

the standard deviation of r normalized by that droplet's mean radius. D is determined for every droplet at every time, and in most of our results below we normalize by the mean value $\langle D\rangle$ within a region. Further details of calculating D are given in the Appendix.

The physical interpretation of D relates to normal stress differences acting on a droplet due to neighboring droplets. More specifically, each droplet is acted on by compression forces from the surrounding droplets. If this compression is isotropic, then it contributes to the pressure on the droplet and does not change D. If the compression is not isotropic, there is a normal stress difference acting across the droplet, and D is an *ad hoc* measure of this. Conceptually, one could consider the Cauchy stress tensor σ acting on a droplet, and rotate the coordinate frame to find the principal normal stresses. In this coordinate frame the off-diagonal elements of the stress tensor are $\sigma_{12} = \sigma_{21} = 0$. If there is a principal stress difference $|\sigma_{11} - \sigma_{22}| > 0$, then this leads to an anisotropic deformation of the droplet into an ellipse-like shape. D is correlated with this principal stress difference. In a coordinate frame rotated by 45° from this one, the shear stress is maximal, and so D is likewise correlated with shear stresses; in fact, the maximum shear stress is mathematically proportional to the principal stress difference. Note that all nonzero deformation is due to forces between neighboring droplets. In experiments done at lower area fractions, below ϕ_J, droplets do not touch one another and all droplets are completely circular ($D = 0$ within measurement error) at all flow rates.

Fig. 1(e) shows the spatial distribution of D at one instant in time. We find that the mean deformation obeys $\langle D\rangle_{y,t}(x) = D_0[1 + A/k_v w(x)]$, with fitting parameters $k_v = 0.81$ mm s^{-1} as a velocity scale and $D_0 = 0.06$ as the deformation for a non-flowing suspension at area fraction $\phi \approx 0.9$. In the absence of flow, $\langle D\rangle_y = D_0$; having $\langle D\rangle_y > D_0$ is because the nonzero flux rate results in droplets being deformed quicker than they can relax (limited by the viscosity). That is, our experiment is *not* in the quasi-static regime, otherwise $\langle D\rangle$ would not depend on the flux A. Nonetheless, the results we find below scale with the average deformation, and do not vary qualitatively from experiment to experiment. While our droplets are out of equilibrium, all relevant time scales (such as time scales for rearrangements) appear to be set by A for our data.

The deformation rises near the walls and near the constriction, where the local shear rates are highest. In most of our analysis

below, we focus on the left side of the sample chamber, where $w(x)$ is large and thus $\langle D\rangle_{y,t}$ is moderately independent of x.

By averaging the deformation of all droplets within a large region as a function of time, we measure the global stress changes $D_G(t)$, as shown in Fig. 2(a). These stress fluctuations are similar to those seen in granular hopper experiments.[5,24,30] In particular, the stress builds up and then can release during a short time interval, with the magnitude of the stress drop fairly significant (in many cases $|\Delta D_{drop}| > 0.2\langle D\rangle$). While our data are insufficient to produce a clean power spectrum, we note that at high frequencies the spectrum is consistent with a power law $P(\omega) \sim \omega^{-1}$. This is true for fluctuations measured either in the left, middle, or right regions of our hoppers. This power-law decay is similar to various constant strain studies on the flow of granular materials[1,24,34–36] which found $P(\omega) \sim \omega^{-1}$ or $\sim \omega^{-2}$, and is suggestive of similarity between our emulsion experiment (with only viscous friction) and these granular experiments (with static and dynamic friction).

These stress fluctuations are related to localized rearrangement events, such as the T1 event shown in Fig. 1(a–c). To illustrate this, in Fig. 2(b) we plot a short segment of the global deformation $D_G(t)$ data from Fig. 2(a). During this time period, we also count the number of T1 rearrangements that occur in the same region, and show the cumulative number in Fig. 2(c).

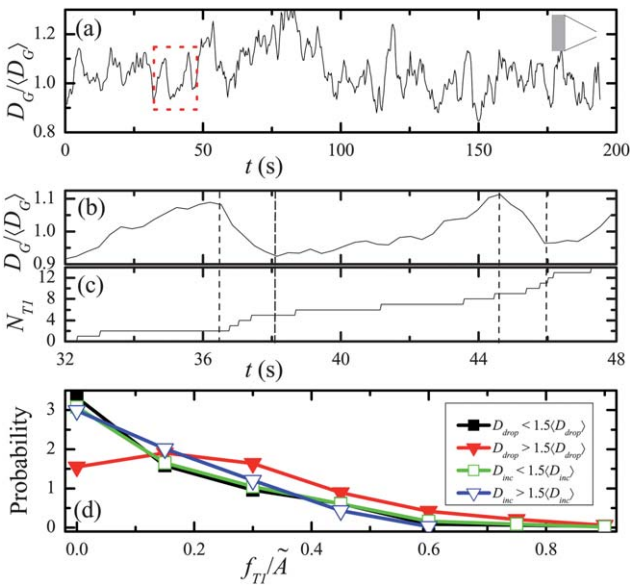

Fig. 2 (a) Temporal fluctuations of the mean global deformation D_G in the left shaded region of hopper as in the inset. This shaded region is ≈ 8 mm in y-extent and so we use $\langle D_G\rangle = \langle D(w = 8\text{ mm})\rangle = 0.087$ to normalize the data. The data are from Run 1 (Table 1). (b) Subset of data from (a) indicated by the red dashed box, showing the fluctuations of the global deformation within the left region of the sample chamber. (c) The cumulative number of T1 events in that region over the same period of time. The vertical dashed lines in (b) and (c) indicate the time intervals when the global deformation significantly drops. (d) The probability distribution of the frequency of T1 events f_{T1} divided by the normalized flux rate $\tilde{A} = A/\pi\langle r\rangle^2$, with the different curves corresponding to different regimes for deformation changes, as indicated in the legend. Open symbols correspond to deformation increases, and closed symbols to deformation drops.

Comparing these two graphs shows that T1 events happen more frequently during periods of large stress drops (36–38 s and 45–46 s). Furthermore, these events are spatially correlated, as shown in Fig. 1(d), which shows the locations of the T1 events occurring between 38 s and 48 s. Clearly one T1 event can trigger rearrangements of other nearby droplets.[2] (We count the T1 events using the algorithm given in the Appendix.)

We define a deformation drop as the magnitude of the decrease of the deformation between a local maximum of $D(t)$ and the subsequent local minimum (although first we smooth the data with a running average over a window of 0.33 s, to reduce maxima and minima which are only due to noise). Further evidence linking large deformation drops to groups of T1 events is found by calculating the frequency of events f_{T1} during a deformation drop. This frequency is defined as the number of T1 events occurring divided by the length of time over which the deformation decreases monotonically. We can similarly define f_{T1} during deformation increases. Probability distributions of f_{T1} are shown in Fig. 2(d) for different sized deformation changes. The solid triangles correspond to the largest deformation drops, and this distribution shifts to higher frequencies. These distributions collapse across datasets when f_{T1} is scaled by the normalized flux rate $\tilde{A} = A/\pi\langle r\rangle^2$, and so Fig. 2(d) shows data from all six runs. Fig. 2(d) shows that large stress relaxations are correlated with bursts of T1 events. Theory suggests that the rate of rearrangements is a useful way to characterize the fluidity of jammed materials,[26] and our observations connect this fluidity to the large stress relaxations.

3.3 Local stress relaxation around individual T1 event

Given the correlation between T1 events and large stress drops (Fig. 2), we examine how a T1 event influences the deformation of nearby (local) droplets D_L. We define $\Delta t = 0$ to be the instant of a T1 event [Fig. 1(b)]. Distances from the event are measured by ΔR, where $\Delta R = 0$ is taken to be the center of the four droplets involved in the T1 event at time Δt, that is, ΔR is measured in a co-moving reference frame. The mean local deformation D_L as a function of ΔR is shown in Fig. 3(a) for several different Δt's both before and after the event. Before, the stress builds up at $\Delta R < 2\langle r\rangle$, where $\langle r\rangle$ is the mean droplet radius; this stress buildup reflects strong deformation of the four droplets that will be involved in the T1 event. At the T1 event, the four droplets involved in the event dramatically decrease their deformation [solid circles in Fig. 3(a)], and quickly this stress release is propagated outward to distances $\Delta R = 6\langle r\rangle$. To quantify this, we consider the quantity $f(\Delta R) = D(\Delta R,\Delta t_1) - D(\Delta R,\Delta t_2)$ using $\Delta t_1 = -0.5$ s and $\Delta t_2 = +0.5$ s. We then compute

$$\lambda = \frac{\int \Delta R f(\Delta R) \mathrm{d}\Delta R}{\int f(\Delta R) \mathrm{d}\Delta R}. \quad (4)$$

If $f(\Delta R) = A\exp(-\Delta R/\lambda)$, then this calculation would yield the decay length λ. For the six runs, we find $\lambda/\langle r\rangle = 3.25 \pm 0.35$ (mean and standard deviation). There is no obvious dependence on any of the experimental parameters, in particular the flux rate. The specific values of λ for each run are listed in Table 1. Our directly observed length scale is comparable to those inferred from a

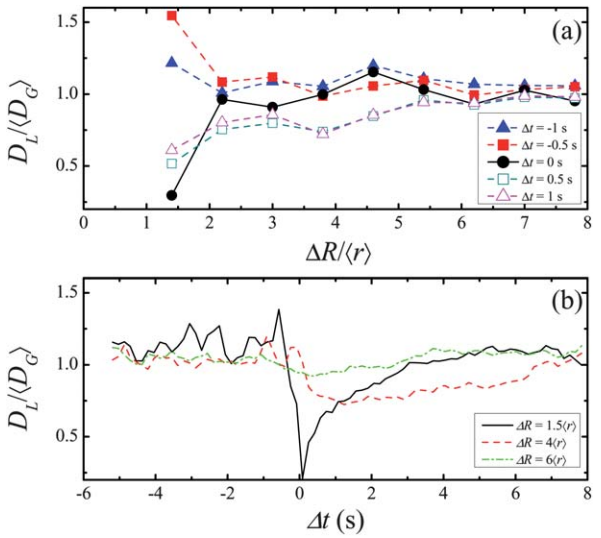

Fig. 3 (a) Mean local deformation D_L around a T1 event, averaging over 186 T1 events during a 194 s duration movie (Run 1). These events all occur in the left side of the channel, see the inset to Fig. 2(a). The distance ΔR is defined in the frame of reference co-moving with the center of the four droplets undergoing the T1 rearrangement; for these data, this frame of reference moves roughly one mean radius per second. The T1 event occurs at $\Delta t = 0$ s. To reduce noise, the data are time-averaged over $\Delta t \pm 0.1$ s. (b) Similar to (a), but as a function of Δt for the given ΔR's as shown. Here the data are spatially averaged over a window of $\Delta R \pm 0.2\langle r\rangle$. For both panels, $\langle D_G\rangle = 0.087$; see Fig. 2 for details.

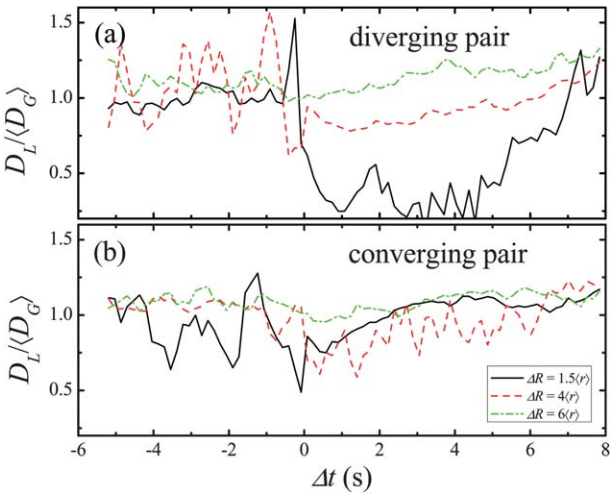

Fig. 4 Similar to Fig. 3(b), but we consider the local deformation D_L averaged along the directions of (a) the diverging droplet pair and (b) the converging pair. These directions are set by considering the instantaneous line joining the converging pair. Droplets within $\pm 45°$ of that line (with the angle measured from the center of the four droplets) are along the converging direction, and the other droplets are along the diverging direction. In this way, space is divided into four equal quadrants, with the orientation of the quadrants changing with time as the T1 event evolves. For both panels, $\langle D_G\rangle = 0.087$; see Fig. 2 for details.

three-dimensional experiment that studied an emulsion with similar polydispersity.[20] Note that our data do not preclude the possibility of power-law decay, for which there would be no length scale, as has been theoretically proposed.[27]

The temporal behavior around a T1 event is shown in Fig. 3(b), where the different curves correspond to different distances ΔR. The black curve shows the changing deformation for the droplets participating in the T1 event. Again, one sees a stress increase prior to the T1 event, a rapid drop at the event, then followed by a slower recovery after the event (likely limited by viscosity). The deformation drop seen in the dashed curve corresponding to $\Delta R = 4\langle r\rangle$ occurs about 0.5 s later in time, suggesting that the stress relaxation diffuses outward, as predicted by theory.[26] Together with Fig. 1(d), the overall picture shown by our data is that T1 events cascade and release stress over a large region, leading to the fluctuations seen in Fig. 2(a). One additional conclusion can be drawn from Fig. 3: the mean local deformation is larger where a T1 event occurs. This is true even before the final increase right before the event; for example, for $\Delta t < -3$ s in Fig. 3(b), for the droplets closest to the future T1 event, $\langle D_L\rangle \approx 1.2\langle D_G\rangle$. The implication is that large stresses are often released at the point they are generated.

Of course, T1 rearrangements have an inherent asymmetry between the diverging and converging droplet directions.[28] To examine this more closely, we separately plot the behavior of D_L as a function of Δt for these two directions in Fig. 4. Here it is evident that the diverging droplets show a much sharper decline in deformation after the T1 event. Droplets in those directions remain less stressed for quite some time after the event. In contrast, the droplets in the converging direction have a relatively rapid recovery of their deformation, approaching the mean value within a few seconds. (For this region of the sample chamber and this run, droplets move roughly one mean radius per second.) The combination of the data in these two directions yields Fig. 3(b), and it shows that the large stress release after T1 mainly comes from the diverging direction. This tendency is consistent among the six runs in Table 1. A similar spatial stress field was found in previous simulation,[28] which did not examine the temporal behavior; Fig. 4 shows that this local stress field also changes with time. From Fig. 3 and 4, our observation confirms predictions linking rearrangements to relaxation of stress over a larger region.[26] Furthermore, Fig. 4 highlights that such stress relaxation is not spatially isotropic, although this result is not surprising. Note that Fig. 3 and 4 show average tendencies; any given T1 event can raise the stress elsewhere, and this is likely one reason why clusters of T1 events occur [Fig. 1(d)]. However, Fig. 3 makes it clear that on average, T1 events do indeed lower the stress of neighboring droplets and Fig. 4 demonstrates that this average tendency is true in both converging and diverging directions. The difference with prior simulations[28] is perhaps that the simulations considered the dry limit ($\phi \to 1.0$) while we have a wetter system ($\phi \approx 0.9$).

Our discussion has focused on T1 events, which are elementary rearrangements within 2D samples. For 3D samples, T1 events would be replaced by more complex rearrangements, for example "shear-transformation zones".[37,38] A more nontrivial difference is that our 2D experiment, every droplet feels a viscous drag force from the top and bottom walls, which would not be present for a flowing 3D sample.[39] Fortunately, as mentioned above the inter-droplet forces dominate over this viscous force. In particular, such viscous forces cannot cause rearrangements in 2D as they do not result in strain differences between neighboring droplets. Thus, it seems plausible that our qualitative observations of local

stress reductions resulting from 2D T1 rearrangements should still be relevant for 3D flowing samples.

4 Conclusions

We have used a quasi-two-dimensional emulsion to investigate the correlation between microscopic dynamics and macroscopic stresses in a dense flow through a hopper. Local rearrangements ("T1 events") occur in bursts and are correlated with large stress releases. We observe a length scale for this correlation, where T1 events result in stress releases influencing droplets as far as three droplet diameters away; this is the first direct observation of the "flow cooperativity length" predicted by theory[20,26] and suggested by previous experiments.[20,23] Our results are for a system without static friction, and it is intriguing that the stress fluctuations we see are similar to those seen in granular experiments.[1,7,24,30] These similarities suggest that the connections we see between individual rearrangements, groups of these rearrangements, and macroscopic stress fluctuations, may be common characteristics of complex fluids under shear for both frictionless and frictional systems.

The overall implication of our results is that discrete microscopic rearrangement events are an important means of reducing and redistributing stress within a flowing material. Clearly there is a strong connection between individual events, cascades of such events, and macroscopic stress fluctuations. The localized nature of the stress reductions after a rearrangement event (Fig. 3) shows that stress fluctuations observed at the boundaries of a container are likely due primarily to rearrangements near such boundaries. While flows of complex materials can often be usefully described by coarse-grained and time-averaged flow fields, it is clear that such averages hide interesting behavior: on shorter length and time scales the rearrangements are proceeded by significantly higher stresses, for example [Fig. 4(a)].

5 Appendix

We describe in more detail our procedures for determining the deformation D and the location of T1 events.

5.1 Algorithm to compute deformation D

First, a droplet is identified from its boundary in the microscope images, where the light is refracted at the interface between oil and water. The raw images are grayscale images, and we determine a threshold intensity to convert the grayscale image to black and white: boundaries are black, and regions of pure oil or pure water are white. We then identify each connected white region in the image, and determine its area (total number of white pixels). Any concave regions are discarded as these are always voids. Additionally regions that are too small are discarded as either being the interstices between oil droplets, or else being oil droplets so small that no useful information can be gained from them. In practice, the area distribution is bimodal and so it is straightforward to determine the cutoff. For the regions that are kept, we determine their centers of mass (giving all pixels comprising the region equal mass). To determine the perimeter, we consider rays drawn from the center of a white region outward at an angle, and identify the first black point encountered as a boundary point. For each droplet, we find 200 boundary points evenly spaced around the center (that is, spaced $\Delta\theta = 2\pi/200$ radians apart), and calculate their distance $r(\theta)$ away from the center. Using this $r(\theta)$ data we can then calculate the mean radius $\langle r \rangle$ and deformation D for each droplet (see eqn (3)).

The chief difficulty of very small droplets is our finite resolution: the perimeter may only occupy a few pixels, and so $r(\theta)$ is only coarsely sampled. One other problem arises when the droplet area fraction ϕ approaches 1. In this case, the voids between droplets become hard to see and this results in imperfect identification of the droplet outlines at their corners. In fact, even to the eye the corners of the droplets appear to be distorted at area fractions above $\sim$0.97. This is not a huge limitation; we expect that our algorithm for finding $r(\theta)$ and thus D works quite well for area fractions up to $\sim$0.97 and is less accurate for higher area fractions.

5.2 Algorithm to identify T1 events

One possibility for identifying nearest neighbor droplets is to use the Voronoi tessellation.[40,41] This partitions space into polygons, where each polygon consists of the points closer to the center of a given droplet than to any other droplet. Droplets whose Voronoi polygons share an edge are then considered neighbors. This works well for monodisperse samples, but is less meaningful for our polydisperse samples. Accordingly, we use the Laguerre (radical Voronoi) tessellation instead.[40–42] For this, when determining for a point which droplet center it is closest to, the Euclidean distance is weighted by the droplets' radii. This results in bigger droplets having larger polygons around them. Neighbors are still those droplets who share a polygonal face. This technique correctly identifies all touching droplets as neighbors.

Knowing all neighbors at all times, the goal is to then identify which neighbor pairs separate and which join together, and the times of these events. Unfortunately, the Laguerre tessellation (like the Voronoi tessellation) is sensitive to noise in the droplets' positions. For example, with a little bit of positional noise, four identical droplets positioned at the corners of a square will flip between the two possibilities of diagonally opposite droplet pairs being neighbors. To avoid over-sensitivity to noise, we require two droplets which are moving apart to not only cease being neighbors, but to also have their separation increase by at least 5% over a time interval of 1 s. Likewise, two droplets which are coming together must start being neighbors and also have their separation decrease by at least 5% over $\Delta t = 1$ s.

Having the information of the "moving apart" droplet pairs and the "coming together" droplet pairs, we search for events where we find two such droplet pairs. The final requirement is that the line segment joining the "moving apart" droplets should intersect the line segment joining the "coming together" droplets. If this condition is met, then the intersection of those two line segments is taken as the position of the T1 event, and the time at which the topological change occurs is taken as the time of the T1 event.

Acknowledgements

We thank S. Devaiah, A. Fernandez-Nieves, S. Hilgenfeldt, X. Hong, Y. Jiang, T. Lopez-Leon, M. L. Manning, N. Xu, and P. J. Young for helpful discussions. This work was supported by

the donors of The Petroleum Research Fund, administered by the American Chemical Society. This material is also based upon work supported by the National Science Foundation (CBET-0853837).

References

1 B. Miller, C. O'Hern and R. P. Behringer, *Phys. Rev. Lett.*, 1996, **77**, 3110–3113.
2 D. J. Durian, *Phys. Rev. Lett.*, 1995, **75**, 4780.
3 M. Dennin, *Phys. Rev. E: Stat., Nonlinear, Soft Matter Phys.*, 2004, **70**, 041406.
4 J. Lauridsen, G. Chanan and M. Dennin, *Phys. Rev. Lett.*, 2004, **93**, 018303.
5 S. Tewari, B. Tithi, A. Ferguson and B. Chakraborty, *Phys. Rev. E: Stat., Nonlinear, Soft Matter Phys.*, 2009, **79**, 011303.
6 M. Dennin and C. M. Knobler, *Phys. Rev. Lett.*, 1997, **78**, 2485–2488.
7 D. Howell, R. P. Behringer and C. Veje, *Phys. Rev. Lett.*, 1999, **82**, 5241–5244.
8 T. S. Majmudar and R. P. Behringer, *Nature*, 2005, **435**, 1079–1082.
9 J. Brujić, S. F. Edwards, I. Hopkinson and H. Makse, *Physica A*, 2003, **327**, 201–212.
10 J. Zhou, S. Long, Q. Wang and A. D. Dinsmore, *Science*, 2006, **312**, 1631–1633.
11 G. Katgert and M. van Hecke, *Europhys. Lett.*, 2010, **92**, 34002.
12 C. S. O'Hern, L. E. Silbert, A. J. Liu and S. R. Nagel, *Phys. Rev. E: Stat., Nonlinear, Soft Matter Phys.*, 2003, **68**, 011306.
13 M. Asipauskas, M. Aubouy, J. A. Glazier, F. A. Graner and Y. Jiang, *Granular Matter*, 2003, **5**, 71–74.
14 B. Dollet and F. Graner, *J. Fluid Mech.*, 2007, **585**, 181–211.
15 A. Kabla, J. Scheibert and G. Debregeas, *J. Fluid Mech.*, 2007, **587**, 45–72.
16 F. Graner, B. Dollet, C. Raufaste and P. Marmottant, *Eur. Phys. J. E: Soft Matter Biol. Phys.*, 2008, **25**, 349–369.
17 P. Marmottant, C. Raufaste and F. Graner, *Eur. Phys. J. E: Soft Matter Biol. Phys.*, 2008, **25**, 371–384.
18 B. Dollet, *J. Rheol.*, 2010, **54**, 741–760.
19 G. Debrégeas, H. Tabuteau and J. M. di Meglio, *Phys. Rev. Lett.*, 2001, **87**, 178305.
20 J. Goyon, A. Colin, G. Ovarlez, A. Ajdari and L. Bocquet, *Nature*, 2008, **454**, 84–87.
21 G. Katgert, A. Latka, M. E. Möbius and M. van Hecke, *Phys. Rev. E: Stat., Nonlinear, Soft Matter Phys.*, 2009, **79**, 066318.
22 M. E. Mobius, G. Katgert and M. van Hecke, *Europhys. Lett.*, 2010, **90**, 44003.
23 G. Katgert, B. P. Tighe, M. E. Möbius and M. van Hecke, *Europhys. Lett.*, 2010, 54002.
24 E. Gardel, E. Sitaridou, K. Facto, E. Keene, K. Hattam, N. Easwar and N. Menon, *Philos. Trans. R. Soc., A*, 2009, **367**, 5109–5121.
25 D. Weaire, J. D. Barry and S. Hutzler, *J. Phys.: Condens. Matter*, 2010, **22**, 193101.
26 L. Bocquet, A. Colin and A. Ajdari, *Phys. Rev. Lett.*, 2009, **103**, 036001.
27 G. Picard, A. Ajdari, F. Lequeux and L. Bocquet, *Eur. Phys. J. E: Soft Matter Biol. Phys.*, 2004, **15**, 371–381.
28 A. Kabla and G. Debregeas, *Phys. Rev. Lett.*, 2003, **90**, 258303.
29 P. Schall and M. van Hecke, *Annu. Rev. Fluid Mech.*, 2010, **42**, 67–88.
30 E. Longhi, N. Easwar and N. Menon, *Phys. Rev. Lett.*, 2002, **89**, 045501.
31 R. Shah, H. Shum, A. Rowat, D. Lee, J. Agresti, A. Utada, L. Chu, J. Kim, A. Fernandez-Nieves and C. Martinez, *Mater. Today*, 2008, **11**, 18–27.
32 K. W. Desmond, PhD thesis, Emory University, 2012.
33 J. C. Crocker and D. G. Grier, *J. Colloid Interface Sci.*, 1996, **179**, 298–310.
34 D. W. Howell, R. P. Behringer and C. T. Veje, *Chaos*, 1999, **9**, 559–572.
35 I. Albert, P. Tegzes, R. Albert, J. G. Sample, A. L. Barabási, T. Vicsek, B. Kahng and P. Schiffer, *Phys. Rev. E: Stat., Nonlinear, Soft Matter Phys.*, 2001, **64**, 031307.
36 K. Desmond and S. V. Franklin, *Phys. Rev. E: Stat., Nonlinear, Soft Matter Phys.*, 2006, **73**, 031306.
37 M. L. Falk and J. S. Langer, *Phys. Rev. E: Stat. Phys., Plasmas, Fluids, Relat. Interdiscip. Top.*, 1998, **57**, 7192–7205.
38 P. Schall, D. A. Weitz and F. Spaepen, *Science*, 2007, **318**, 1895–1899.
39 E. Janiaud, D. Weaire and S. Hutzler, *Phys. Rev. Lett.*, 2006, **97**, 038302.
40 H. Telley, T. M. Liebling and A. Mocellin, *Philos. Mag. B*, 1996, **73**, 395–408.
41 B. Gellatly, *J. Non-Cryst. Solids*, 1982, **50**, 313–329.
42 F. Aurenhammer, *SIAM J. Comput.*, 1987, **16**, 78–96.

